The Effect of Horizontal Grid Resolution in an Atmospheric Circulation Model[1]

K. MIYAKODA, R. F. STRICKLER, C. J. NAPPO, P. L. BAKER AND G. D. HEMBREE

Geophysical Fluid Dynamics Laboratory, NOAA, Princeton University, Princeton, N. J.

(Manuscript received 15 January 1971, in revised form 22 February 1971)

ABSTRACT

Truncation error of the numerical solution in a circulation model is still one of the most serious sources of error for the extended-period prediction. Different grid intervals are taken and the behavior of the solution is studied empirically. The meshes for the hemispheric domain are $N=20$, 40 and 80, where N is the number of grid points between the pole and the equator on the stereographic projection map. Analysis revealed that finer meshes provide clearly better solutions even for the planetary-scale mode, and the $N=80$ solution is definitely different from the $N=40$ beyond about 6 days. Further comparisons were made to see if the $N=80$ solution is actually closer to observation. The results were encouraging. Promise is seen for improvement in the forecast to about 10 days. The inclusion of subgrid-scale eddy viscosity, which seems to be necessary when applying a grid to the flow field, is also examined.

1. Introduction

One serious defect in previous numerical weather predictions is that the meandering in the computed westerlies was appreciably weaker than in the observed and that cut-off lows were seldom produced. This is not a feature peculiar only to the particular prediction model we are using. It is straightforward, perhaps, to assume that this defect is related to insufficient grid resolution and to excessive horizontal eddy viscosity. If so, the following questions should be answered. How much grid resolution is needed? And what is a reasonable lateral Austausch coefficient? Of course, ideally it is desirable that the mesh be as fine as possible, since atmospheric flow contains a continuous spectrum of wavelengths down to molecular size.

However, there may be a finite grid mesh which gives a satisfactory solution from a practical standpoint, if the scale of interest is confined to a certain range and if the prediction period is limited. Experience shows (Charney *et al.*, 1950) that a fairly large grid interval, say 400 km, may represent the cyclone-scale disturbances with enough accuracy for a one-day forecast.

We are concerned now, however, with higher accuracy and with integration for longer periods of time, so the adequacy of the grid resolution has to be re-examined.

2. Background

According to the empirical study of Grammeltvedt (1969) with a barotropic equation, more than 15 grid points per wavelength are probably needed for time integrations >3 days. Miyakoda (1960) also showed the necessity of a large number of grid points per wavelength (particularly for the two-dimensional, nonviscous vorticity equation) and showed that the further the integration period is extended, the higher the resolution required. Clusters of vorticity given initially are stretched as the computation proceeds. Eventually the extremely elongated vorticity filaments can no longer be resolved by the grid. Then the "spaghetti" (or "cascade") effect occurs (Platzman, 1961), which leads to a kind of numerical instability (Phillips, 1959).

Arakawa (1966) designed a scheme of finite differencing in which the formulation is based upon integral constraints on the quadratic quantities, i.e., kinetic energy and squared vorticity. With this device he succeeded in avoiding the instability. As mentioned above, the stretching of the vorticity is a physical reality, and the "spaghetti' effect is a computational result. In nature molecular viscosity supposedly dissipates the very narrow vorticity filaments.

In a grid calculation, a certain spectrum is truncated by the mesh. This subgrid-scale effect can be effectively compensated by including an eddy viscosity. Phillips (1956), in his numerical experiment of the general circulations of the atmosphere, used Richardson's $\frac{3}{4}$ power law hypothesis for determining the eddy viscosity coefficient. Smagorinsky (1963) formulated the nonlinear viscosity term, which yields more scale-selective dissipation than the linear viscosity term. This pseudo-viscosity is derived conceptually as the consequence of applying a grid to the flow field, but it is also true that this viscosity is a great help in achieving computational stability.

In the circulation model which is used in the present study, Lilly's finite-difference scheme is adopted together with the nonlinear viscosity of Smagorinsky

[1] Paper presented at the AMS–IMS International Conference on Meteorology, Israel, 30 November–4 December 1970.

et al. (1965). The problem is now to simulate three-dimensional baroclinic flow. The integrations differ from the two-dimensional experiments described above in that the clusters of vorticity tend to be well organized and preserved for a considerable span of time. This is achieved by the continual intensification of vortex tubes resulting from the vertical stretching and the weakening of the stretched filaments by viscous dissipation. It may be remembered that early operational numerical forecasts with the barotropic model suffered from a tendency for damping of the wave patterns even in the 24-hr forecast. This was due to the lack of a vorticity source and to unlimited horizontal stretching of vortex filaments.

Thus, the most important points in the numerical computation of atmospheric motion in the grid system are probably those of accurately representing the strengthening process of vortices (baroclinicity) and the proper inclusion of the parameterization of eddy dissipation.

Recently Manabe *et al.* (1970) compared the results of the general circulation model for two different horizontal meshes; the grid sizes at mid-latitudes were approximately 500 km and 250 km ($N=20$ and $N=40$). The study revealed clearly that the high-resolution model provided much improved results in many respects; in particular, the detailed structure of fronts became more realistic. It was also shown that the rate of baroclinic energy conversion was increased by 13%. Furthermore, in the refined version of the model, the wavelength at which subgrid-scale dissipation is most effective is shifted toward a smaller scale, though probably not small enough. Wellck *et al.* (1971) also made a similar experiment, the conclusion being similar.

3. The basic circulation model

The basic equations used in this study were described in the papers by Smagorinsky *et al.* (1965) and Manabe *et al.* (1965). In particular, the model used for Experiment 3 reported in Miyakoda *et al.* (1969) is more nearly like the one used here. The only differences are that in the present study the grid resolution and the coefficient for horizontal eddy viscosity are varied.

The model takes the equations of motion for the rotating system and the hydrostatic assumption, and includes nine vertical levels. Also included are the radiation processes, water vapor and its condensation processes, and the effects of orography and land-sea contrast.

The equations of motion and the thermal equation include the nonlinear viscosity terms F_x, F_y and F_θ, defined as (Smagorinsky, 1963):

$$F_x=m^4\left[\frac{\partial}{\partial x}\left(\frac{\gamma}{m^2}D_T\right)+\frac{\partial}{\partial y}\left(\frac{\gamma}{m^2}D_S\right)\right], \tag{3.1}$$

$$F_y=m^4\left[\frac{\partial}{\partial x}\left(\frac{\gamma}{m^2}D_S\right)-\frac{\partial}{\partial y}\left(\frac{\gamma}{m^2}D_T\right)\right], \tag{3.2}$$

$$F_\theta=m^2\left[\frac{\partial}{\partial x}\left(\frac{\gamma}{m^2}\frac{\partial\theta}{\partial x}\right)+\frac{\partial}{\partial y}\left(\frac{\gamma}{m^2}\frac{\partial\theta}{\partial y}\right)\right], \tag{3.3}$$

where u and v are the wind speeds in the x and y directions, respectively, on the stereographic projection map, θ is the potential temperature, and

$$D_T\equiv\frac{\partial u}{\partial x}-\frac{\partial v}{\partial y}, \tag{3.4}$$

$$D_S\equiv\frac{\partial v}{\partial x}+\frac{\partial u}{\partial y}, \tag{3.5}$$

$$|D|=\sqrt{D_T{}^2+D_S{}^2}, \tag{3.6}$$

$$m=\frac{2}{1+\sin\varphi}, \tag{3.7}$$

$$\kappa=R/c_p, \tag{3.8}$$

$$\gamma=l^2|D|, \tag{3.9}$$

$$l=\frac{1}{\sqrt{2}}\frac{k_0\Delta s}{m}. \tag{3.10}$$

In the above m is the map-scale factor for the stereographic projection map, φ the latitude, R the gas constant, p the pressure, c_p the specific heat at constant pressure, γ the Austausch coefficient, l the characteristic length which is related to the spacing of the lattice, D the deformation, Δs the space increment relative to the earth, and k_0 the proportionality constant of the eddy viscosity term which will be discussed in the next section.

The vertical eddy viscosity is not included above 700 mb and is assumed only for u and v in the layer below the 700-mb level.

4. Horizontal eddy viscosity

The value $k_0=0.4$ which coincides with the von Kármán constant has been extensively used in studying the general circulation of the atmosphere (e.g., Smagorinsky *et al.*, 1965; Manabe *et al.*, 1965, 1970). Lilly (1967, 1970) attempted to find a physical interpretation of the coefficient in the light of the isotropic turbulence theory. Following his derivation one has

$$\frac{k_0}{m}\approx 0.21. \tag{4.1}$$

This value is considerably smaller than 0.4. [Lilly (1967) and Deardorff (1971) used the notation c which is equal to k_0. The definition of deformation is different from that in this article by $\sqrt{2}$. According to Deardorff, the recent revised value of c for *three-dimensional* flow is 0.20].

On the other hand, even before we knew of Lilly's discussion, there was some doubt about the adequacy

of the value $k_0=0.4$. To test the suitability of the value, a number of experiments were carried out by varying k_0 in steps from 0.4 through 0.1. With the $N=40$ model, 14-day predictions were repeated for each k_0 for the case of 1200 GMT 9 January 1964. It was seen from the computed hemispheric maps of geopotential height that the wiggling in the pattern increases with the decrease of k_0, and that the cut-off low tends to be better formed as k_0 decreases.

To quantitatively assess the influence of k_0 on the flow field, the ratio of the zonal kinetic energy K_Z and the eddy kinetic energy K_E is taken at level 4($\sim$336 mb); K_Z and K_E are defined by

$$K_Z=\int\int \frac{1}{2}\rho(\bar{u}^2+\bar{v}^2)a^2\cos\varphi d\lambda d\varphi, \tag{4.2}$$

$$K_E=\int\int \frac{1}{2}\rho(u'^2+v'^2)a^2\cos\varphi d\lambda d\varphi, \tag{4.3}$$

where the bar notation is the zonal average and the primed variable is the deviation from the average, λ the longitude, ρ the air density, and a the radius of the earth. The domain of integration is north of 20N.

Fig. 1 is the time variation of the ratios during the 14-day period. The observed value is the thick solid line and remains around 1. On the other hand, the ratios for $k_0=0.4$, 0.3, 0.2 are noticably larger than 1, suggesting that perhaps the viscosity is too large, smoothing the detailed structure of vortices excessively. Thus, it appears that k_0 should be less than 0.1, so far as this measure is concerned. It should be mentioned, however, that despite the closeness of K_Z/K_E to unity the large-scale feature of the flow pattern is not greatly improved.

It may be wise, however, to hold some reservations about this conclusion, since the horizontal resolution is still relatively coarse ($N=40$); thus, the more general requirement for k_0 may not apply to this particular case. In addition, the grid-cut in the spectral space is far above the so-called inertial subrange, and the spectral function in this region is somewhat different from $k^{-5/3}$. [Leith has now postulated a k^{-3} relationship for the quasi-two-dimensional flow (see Ogura, 1958, and Leith, 1968).]

Anyway, the overall impression obtained from this test is that k_0 should be smaller. However, the "wiggling" in the case of $k_0=0.1$ increases so appreciably that the calculation could not be continued beyond the 9th day. There are two major potential factors that may remove this difficulty; first, a more stable scheme of finite differencing, and second, a reduction of the shock generated by the present moist convection scheme, where "shock" means a suddenly created imbalance between the mass and velocity fields.

Grammeltvedt (1969) tested a number of finite-difference schemes, and concluded that the generalized

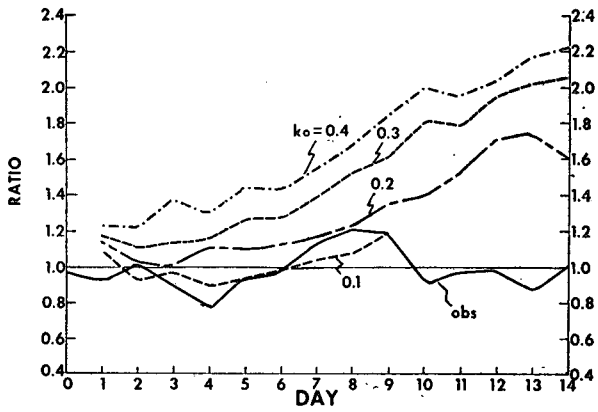

FIG. 1. Time variation of K_Z/K_E as a function of k_0, the coefficient of the horizontal nonlinear viscosity.

Arakawa method (in which not only the kinetic energy but also the squared vorticity for the nondivergent component of flow are conserved) and Shuman's method (1960) are the best among those tested from the standpoint of computational stability. (The present scheme in our model conserves kinetic energy but not the squared vorticity.) Concerning the shock, it appears that the small-scale convection process is responsible. A new process could be designed in which the amount of shock is reduced (Gadd and Keers, 1970).

In all subsequent experiments k_0 is set to 0.25 as a practical compromise based upon the experience described above.

5. Horizontal grid resolution

Another series of tests were undertaken to determine the effect of changing the resolution of the horizontal grid. Like the test of instrumental apparatus in a laboratory experiment, it is important and imperative to know the mathematical performance of the numerical model.

a. Grids

Three mesh sizes were taken, i.e., $N=20$, 40 and 80, where N is the number of grid points between the pole and the equator on the stereographic projection map. The $N=20$, $N=40$ and $N=80$ meshes consist of 1257, 5025 and 20,081 grid points, respectively, for each level. The corresponding grid lengths at the pole are 640, 320 and 160 km; those at the equator are just half the above; while the distances at the mid-latitude are 540, 270 and 135 km. By comparison, the grid conventionally used in the National Meteorological Center in Suitland (NMC) corresponds to $N=31.2$, where the grid distance at the pole is 381 km.

b. Computation times

The time increment Δt is 10.0, 5.0 and 2.5 min for the $N=20$, 40 and 80 models, respectively. The com-

putation time is 1 hr per one-day forecast with the $N=20$ model, 12 hr with the $N=40$, both with the UNIVAC 1108 machine, and 16 hr for $N=80$ in the IBM 360/91. The codes of the $N=80$ model are quite different from those of the $N=40$ model (for efficiency), though the physical processes are exactly the same.

c. Marching calculation

In the marching computation for the 14-day prediction, the "leapfrog" method is normally used, but computational irregularity appears near the equatorial boundaries, and sometimes the computation cannot be continued further. This happens only in the $N=40$ and $N=80$ models, not in the $N=20$, suggesting that shock generation due to "convective adjustment" is larger in the high-resolution model. In such a case, the "Euler backward method" is applied to damp out the high-frequency mode of the solution (Matsuno, 1966; Mintz, 1965; Kurihara, 1965). This process is used for only a short period in order to avoid unnecessary filtering. For $N=40$, it is applied for a period of 0.5 day at the 10th day, and for $N=80$, it is used for a period of 0.25 day at about 4.5, 8.5 and 12 days. Apparently the amount of damping that results does not depend upon the time interval but on the number of time steps (Kurihara, 1965).

d. The cases

Two cases of data were used for this study. One was for the 2-week period which began 1200 GMT 9 January 1964, and the other for the period which began 1200 GMT 4 January 1966. They are the same cases adopted by Miyakoda *et al.* (1969).

e. Comparison

The ideal evaluation of the mathematical performance of a system of finite-difference equations is to compute the true solution for the equations and then compare the numerical solution of the finite-difference equation with the true solution. This is, however, extremely difficult, if not impossible. Instead, we have made a comparison between the solutions obtained with the model at different resolutions, studying their differences as well as their departures from reality.

In the following, we shall discuss two aspects of the comparisons: first, the transient behavior of the flow for the two-week period of prediction, and second, the general circulation features which are defined as temporal averages of quantities such as the zonal wind, eddy kinetic energy, moisture distribution and mean temperature.

6. Two-week evolution of flow fields

a. Hemispheric geopotential maps

1) 500 mb

The height fields for the observation and the $N=80$, $N=40$ and $N=20$ predictions are displayed (1964 case) in Figs. 2 and 3. The $N=20$ result is already quite different from $N=40$ even at the 4th day. As far as $N=40$ and $N=80$ are concerned, the general features are similar, but there are definite differences in the local configurations of trough and ridge—particularly with respect to the troughs over the United States and the Caspian Sea. The greater similarity of the $N=40$ and $N=80$ predictions suggest that with the increase of resolution the numerical result is apparently converging toward a certain solution (supposedly the true solution of the equations). This fact is important because it shows that the result contains more than just truncation error. By comparing the prediction with the observed fields one may see that overall the $N=80$ result approaches the observed more closely, though obviously a very close coincidence cannot be expected at this stage of the evolving prediction system.

It is interesting to note the sharp trough over the Caspian Sea that appears in the $N=80$ map on day 4. It can be identified in the observed map, but it is nearly missing in the $N=40$ map. In general, experience has shown that an existing trough cannot be better defined by reducing k_0 further, even below 0.1; the reduction of k_0 apparently leads to the formation of a cut-off low, if there is already an established trough, but it does not create a new trough. On the other hand, refinement of the mesh does give rise to another trough which is virtually missing in the $N=40$ case.

With the increase in resolution, the westerlies undergo meandering, and the jet streams are sharper. The result of the $N=20$ model is particularly poor in this respect. A close look at the $N=80$ map reveals that cyclones and anticyclones at high latitudes are quite detailed, indicating that polar fronts are reproduced more realistically in the $N=80$ than in the $N=40$ map.

These characteristics are even clearer at the 8th day (Fig. 3). The large-scale configuration of the wave pattern at $N=40$ is appreciably different from that at $N=80$, suggesting that the $N=40$ result is not a good approximation to the solution for the 8th day.

If one looks at the local detail, the result of a higher resolution model is not always better. But an overall feature is that the solution improves with increasing resolution. For example, it may be seen at the 4th day that the behavior of a cyclone over the United States turns out to be good at $N=40$ but not as good as at $N=80$. Whatever the agreement is, however, $N=80$ should be the better solution in the sense that the truncation error is supposedly less.

2) 1000 mb

Fig. 4 is a similar comparison, for the 1000-mb maps at the 8th day (1964 case). The effects of the finite-difference resolutions on the results is more evident in these maps than at 500 mb. The most striking feature is that the vortices are better grouped and located. The positions of the major anticyclones are considerably improved, but the cyclones at higher latitudes are not.

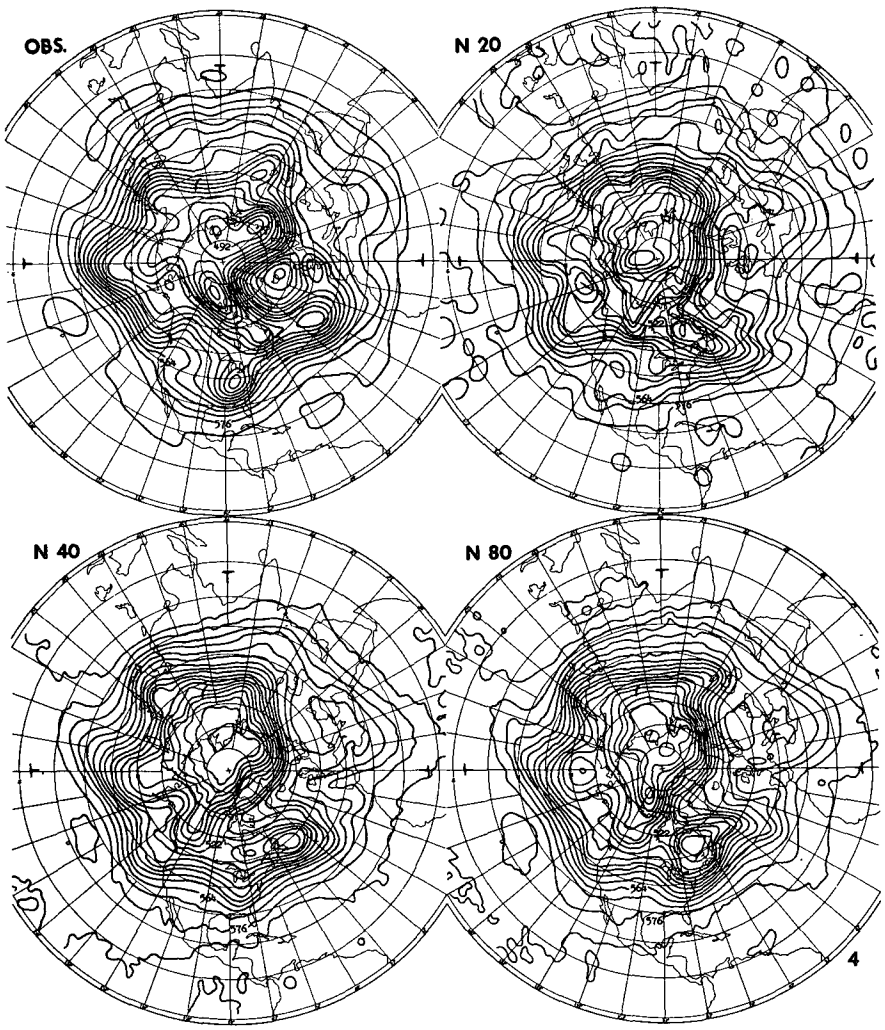

FIG. 2. The 500-mb geopotential heights on the 4th day. The height is in units of 10 m, the contour interval 60 m.

3) Remarks

Several earlier studies have used models of high-computational resolution. Thus, Howcroft (1966) and Gerrity and McPherson (1969) used a grid size of 190.5 km at 60N, while Bushby and Timpson (1967) employed a staggered grid with a size of 40 km. Since all were concerned with the small-scale or mesoscale forecast for a limited area (instead of the hemisphere), and the time periods of their forecasts are short, their purpose was not quite the same as that of the present study. They reported that mesh refinement significantly improves the quality of a short-range forecast. The curvature of height contours in troughs is well maintained. In the 10-level model of Bushby and Timpson, frontal rainfall is well simulated (Benwell and Bushby, 1970).

b. Trough-ridge diagram

To get a comprehensive view of the transient features of atmospheric motion, the trough-ridge diagram (Hovmöller) is useful. This is a longitude-time chart of geopotential height taken along a certain latitude circle. Fig. 5 shows 500-mb heights for the 1964 case for the latitude zone between 35 and 45N.

An obvious fact is that the streaks of the troughs or ridges run more vertical for $N=20$, less for $N=40$ and least for $N=80$, indicating that the travelling waves have lower speeds in the $N=20$ and higher speeds in $N=80$ models. In this respect as well as in other fine details, $N=80$ compares more favorably with the observed. One exception is that at the end of the prediction period, i.e., on 12th day (indicated by the arrow at the side) the wave behavior is appreciably disturbed in the $N=80$ results.

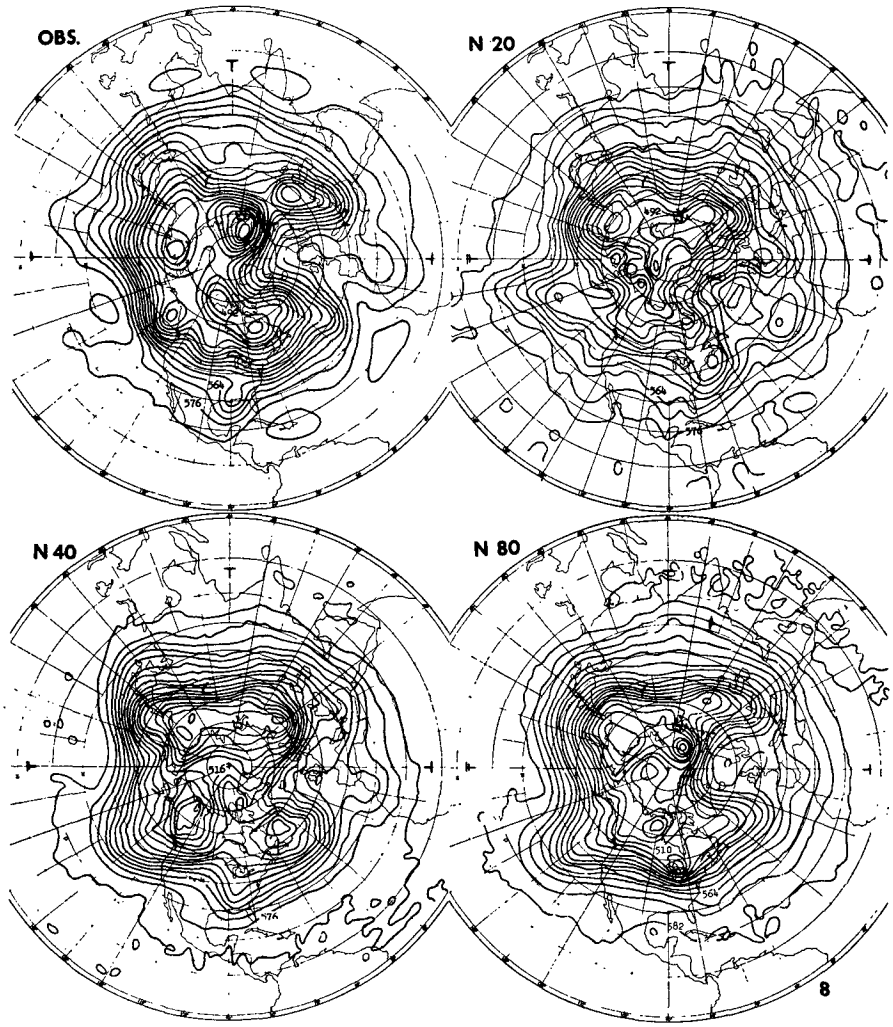

FIG. 3. The 500-mb geopotential heights on the 8th day.
The interval and units are the same as in Fig. 2.

In hope of getting deeper insight, a spectral analysis of the trough and ridge pattern was made. The zonal distributions of the 500-mb geopotential height for each day were decomposed by the Fourier method. The components were then grouped into three parts, i.e., wavenumbers 1 and 2, 3–5, and 6–10. A separate trough-ridge diagram was then reconstructed (in physical space) from each group of spectral components (Figs. 6–8).

Wavenumbers 1 and 2 (the "ultra-long waves") and the second group of wavenumbers 3–5 (the "very long waves") are usually called Rossby waves or planetary waves. The third group comprise the "cyclone waves" which are baroclinically very unstable in conventional theory [see, for example, Saltzman and Fleisher (1960) and Phillips (1963) for the wave classification].

In wavenumbers 1 and 2 (Fig. 6), there is a marked difference between $N=20$ and $N=40$. Perhaps it is surprising that the effect of grid resolution is serious in the regime of the lower wavenumbers. As the grid interval decreases, the westward travelling waves become more pronounced with amplitudes considerably increased.

The spurious retrogression of ultra-long waves was experienced routinely in numerical weather prediction during the late 1950's, and the cause was intensely discussed (Wolff, 1958; Cressman, 1958; Wiin-Nielsen, 1959). There are two modes of the wave. One is the free mode which propagates horizontally and corresponds to the theoretical Rossby-Haurwitz wave. The other is the forced mode which is quasi-stationary and is conceivably related to the effect of orography and the distribution of land and sea (Charney and Eliassen, 1949; Smagorinsky, 1953; Gilchrist, 1953; Murakami, 1956, 1964; Martin, 1958; Staff members, Academia Sinica, 1958; Saltzman, 1963; Döös, 1962; Sankar-Rao, 1965; Derome and Wiin-Nielsen, 1971).

According to Kubota and Iida (1954), Deland (1964,

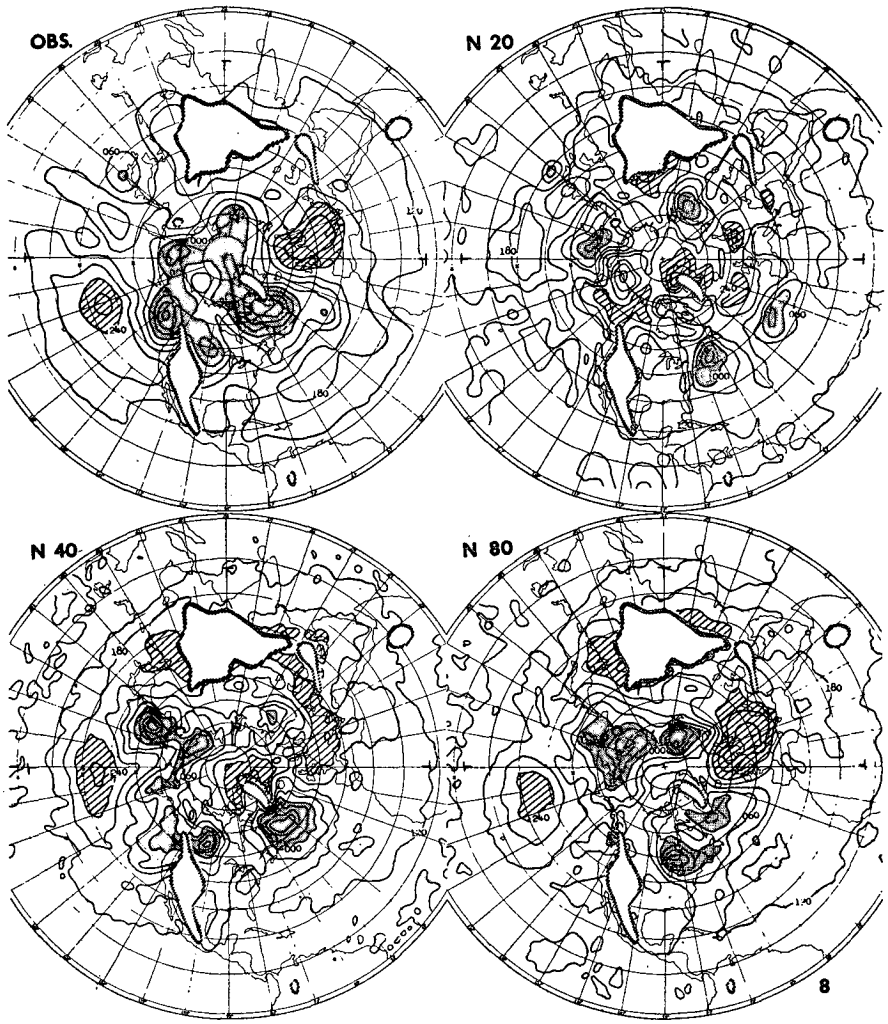

FIG. 4. The 1000-mb geopotential heights on the 8th day. The anticyclone areas with height values >240 m are hatched, and the cyclone areas with values <0 m are stippled. The loci of small segmented lines mark the mountain areas.

1965), Eliasen and Machenhauer (1965), and Kao and Wendell (1970), the free mode certainly exists in nature together with the forced mode mentioned above. But the early numerical models failed to compute the amplitude of the free mode correctly, probably due to the crude treatment of the time change in the surface pressure. Also they failed to compute accurately the topographical influence and the sensible heat flux from the earth's surface.

The present study demonstrates another point which has been overlooked. Coarse resolution does not compute the correct amplitude of the forced mode. It is very encouraging that refinement of the grid improves the stationary mode, probably due to the more correct calculation of energy conversion due to the baroclinic instability as well as the eddy energy conversion due to the barotropic process.

Yet even in the result of the $N=80$ model, the amplitude is still underestimated. The question is whether the resolution of $N=80$ is insufficient or whether some missing physical process is responsible for the underestimation.

The very long waves (Fig. 7) are the most dominant in the spectrum space of geopotential height. Interestingly, the major wave packets propagating at group velocity, as seen in the total trough-ridge diagram (Fig. 5), are largely contributed by these wavenumbers (see the plotted arrows in Figs. 5 and 7). The group velocity of Rossby waves mentioned in previous works, for example, those of Reiter (1958), van Loon (1965) and Platzman (1968), was about 30° longitude per day (eastward), which is just about the same as in Fig. 7. One may easily understand that the production of this wave energy and its propagation are the most dominant factors in the evolution of weather, and therefore, that they are the most important items in extended-range prediction. However, this point is not clearly reproduced in the present study.

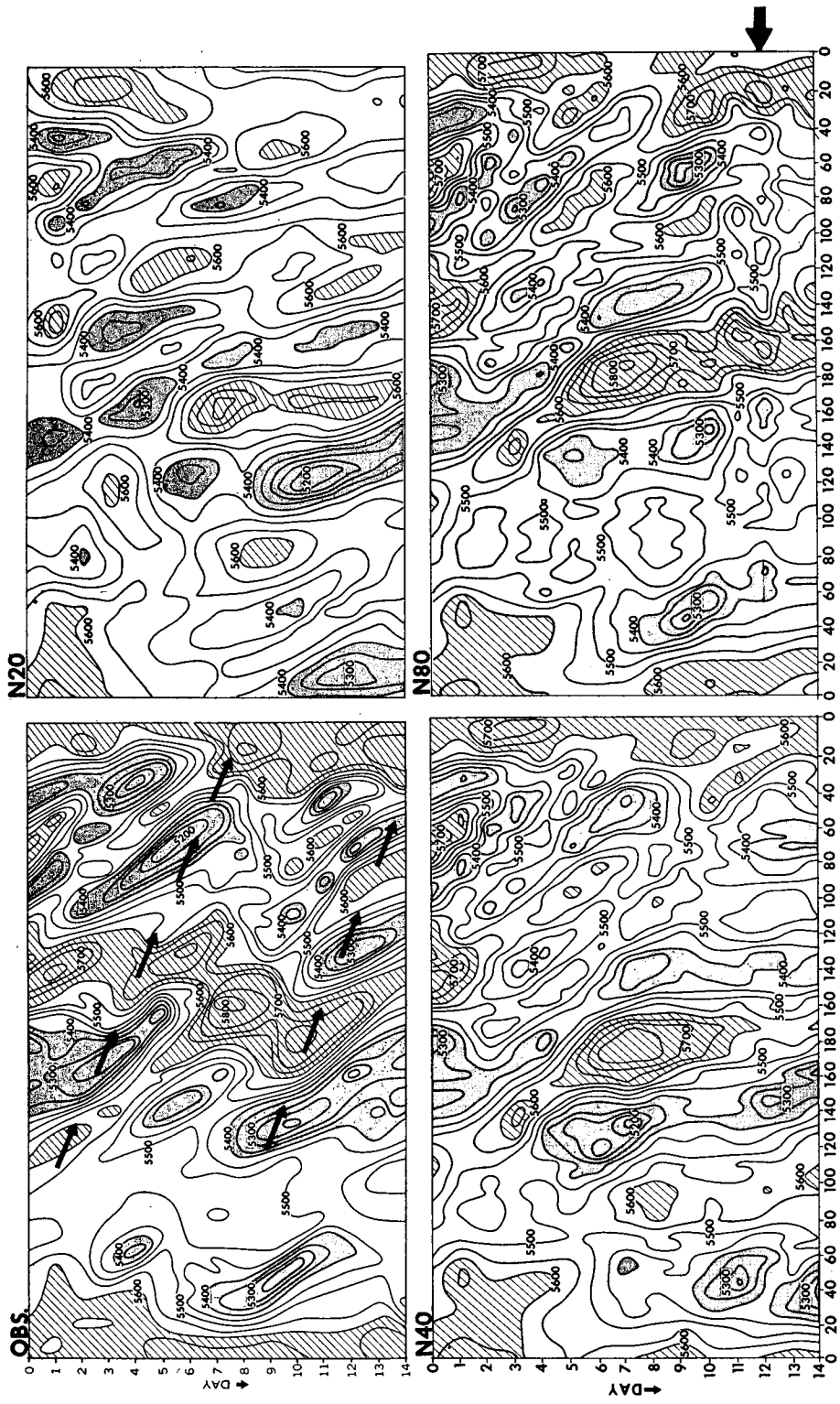

FIG. 5. The 500-mb trough-ridge diagrams, in meters, for the latitude zone between 35 and 45N. The ordinate indicates the time from 0 through 14 days. The ridge areas with geopotential height values >5600 m are hatched, and the trough areas with values <5400 m are stippled. Plotted arrows show movement of wave packets at the group velocity.

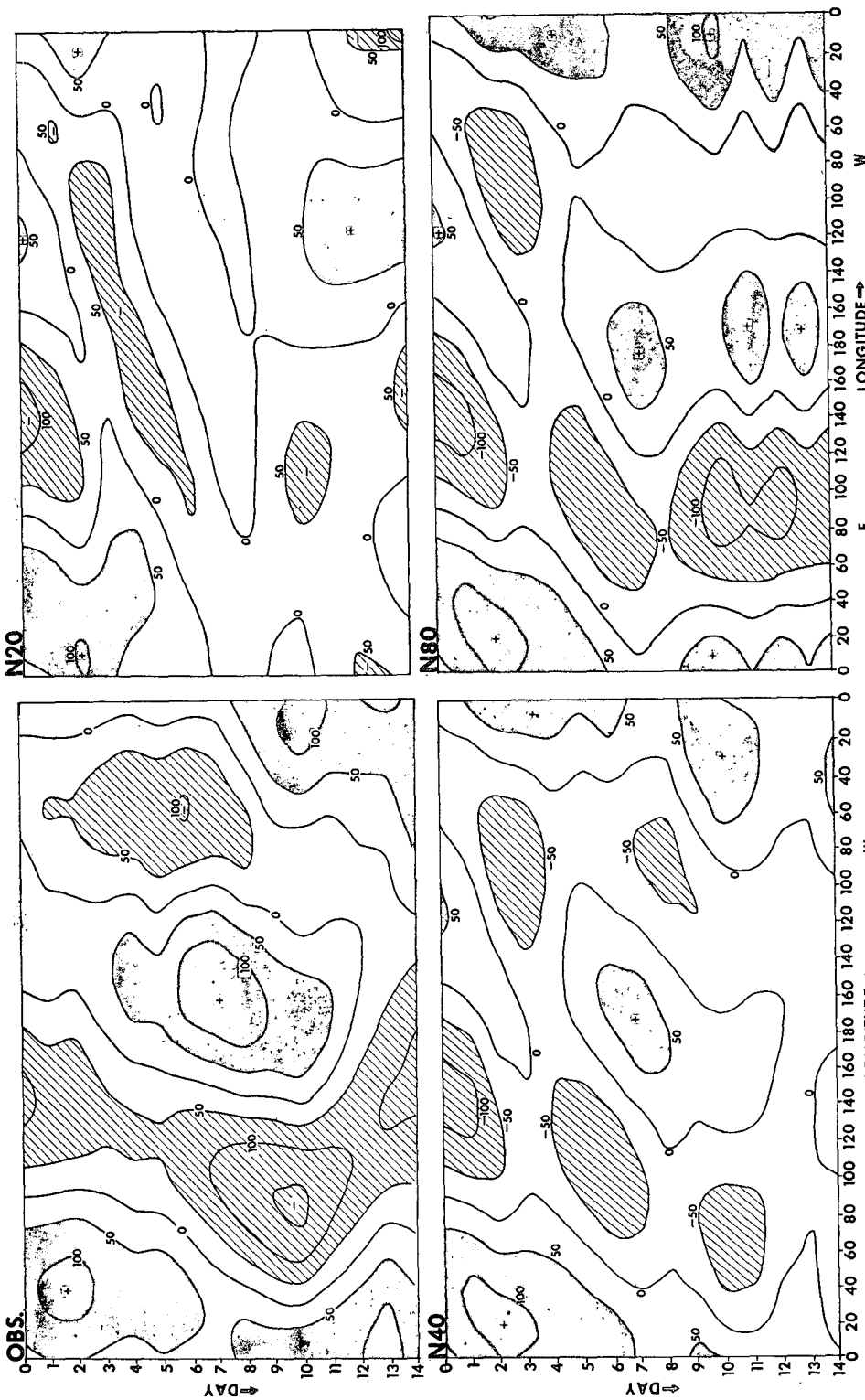

FIG. 6. The synthesized trough-ridge diagrams, with contours in meters, for wavenumbers 1 and 2.

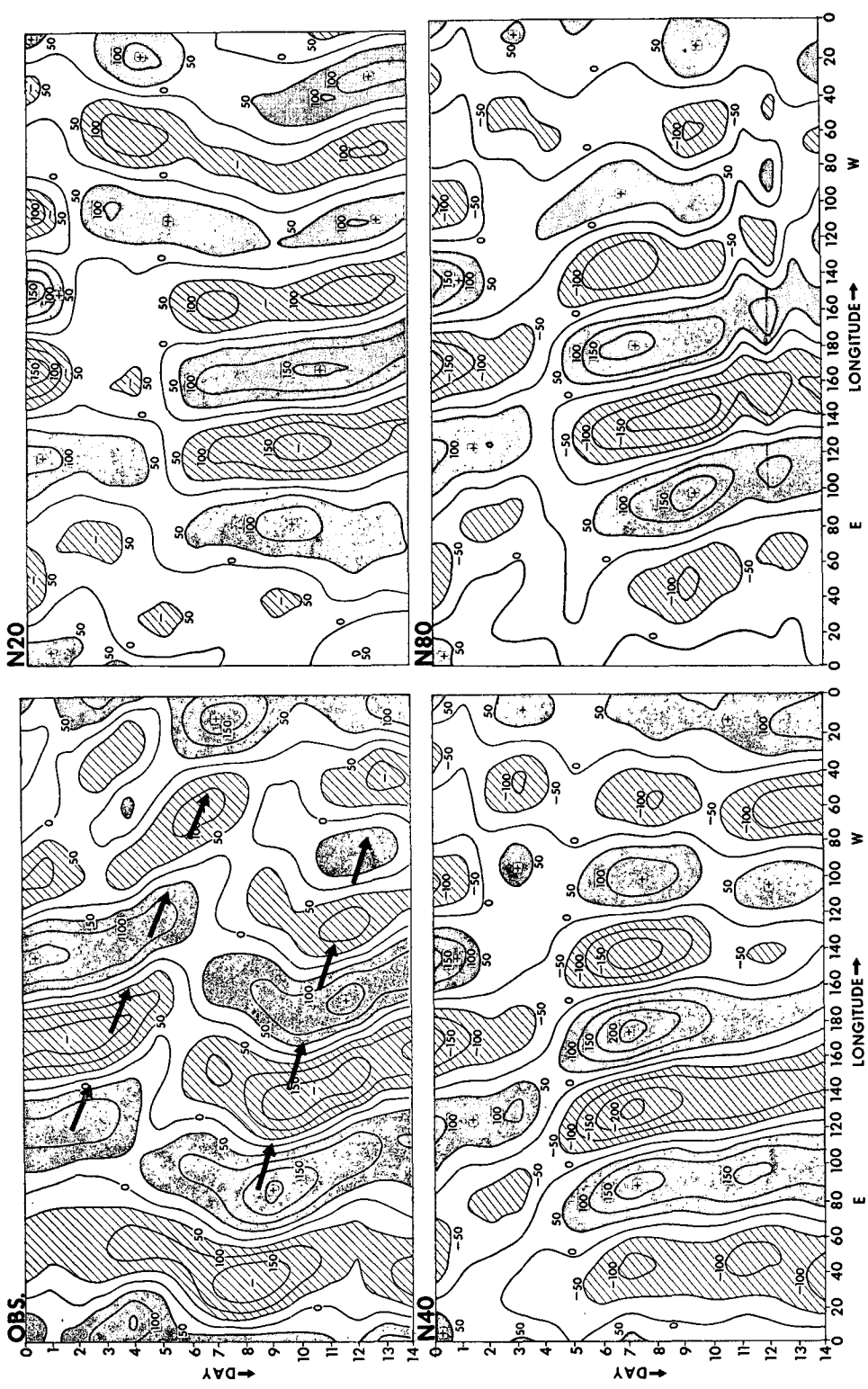

FIG. 7. Same as Fig. 6 except for wavenumbers 3–5. Arrows again show motions of wave packets.

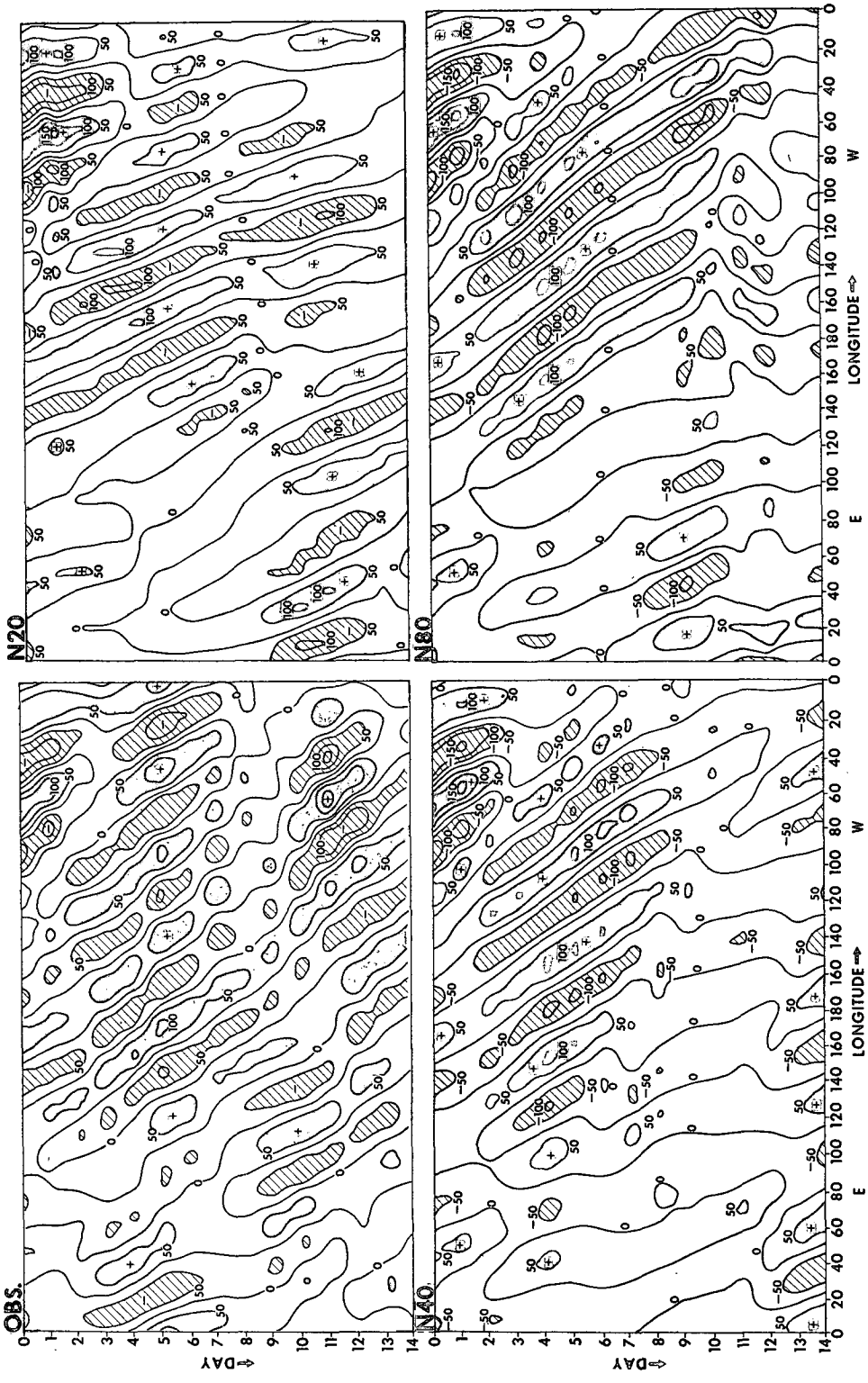

FIG. 8. The synthesized trough-ridge diagrams for wavenumbers 6–10.

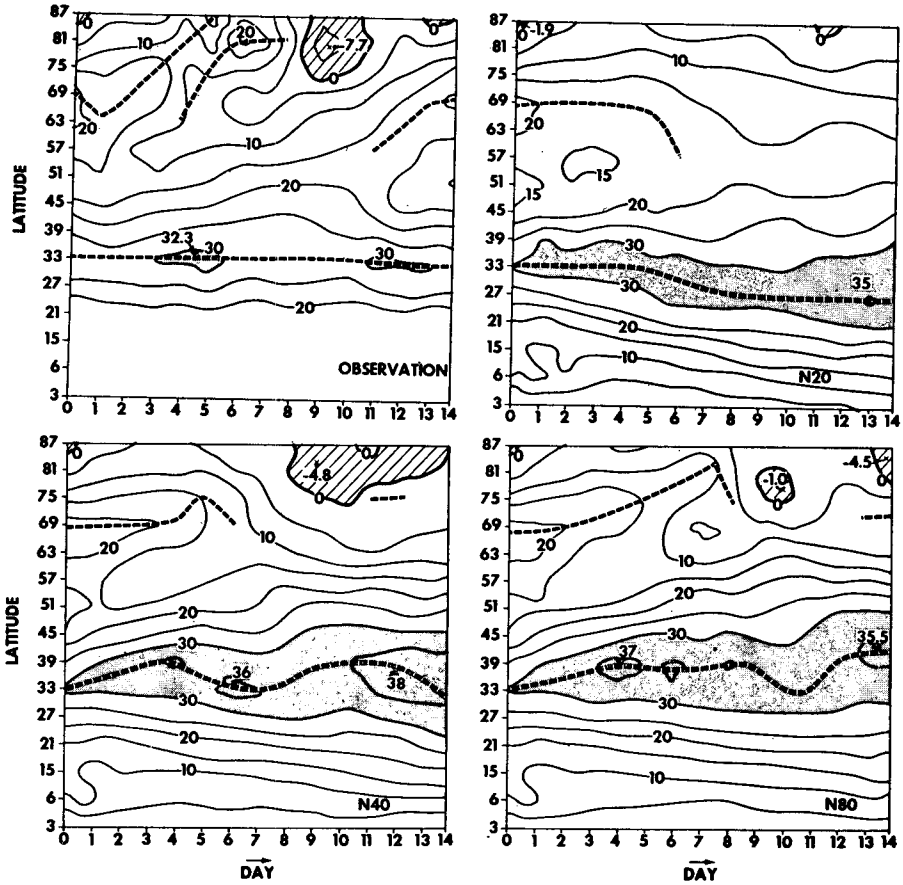

FIG. 9. The zonal wind at level 3 (~189 mb). The westerlies are positive. The abscissa is time from 0 through 14 days, and the ordinate is latitude. The jet maxima are connected with thick dashed lines. The regions where the wind intensity >30 m sec^{-1} are stippled. The regions of easterlies are hatched.

In a statistical study of the performance of the $N=40$ model, it was noted that the greatest shortcoming in the solution is the underestimation of amplitudes of wavenumbers 1–3. One of the important factors causing this is the grid resolution. Truncation error manifests itself in the fact that baroclinicity is not well represented, and the nonlinear decascade process which simultaneously carries energy from the smaller to the larger scales is greatly distorted (see Fjørtoft, 1953; Saltzman, 1959; Saltzman and Fleisher, 1960).

An analysis of the model atmosphere by Manabe *et al.* (1970) shows in the low-resolution model ($N=20$) that the baroclinic conversion from eddy available potential to eddy kinetic energy ($-\overline{\omega'\alpha'}$) is underestimated at low wavenumbers. Also their results indicate that the barotropic energy exchange between different wavelengths increases markedly with increasing resolution (also see Section 7).

One effect of truncation error, now well known to be false, is that of phase speed. In the usual finite-difference method, that is, centered in space with "leap-frog" differencing in time, the computed wave becomes dispersive spuriously, and the phase speed appears smaller as the resolution decreases (Magata, 1957; Reiser, 1957; Økland, 1958; Kurihara, 1965). This property is clearly demonstrated in Fig. 8 (Kurihara's analysis showed that the Euler backward process causes phase speed to accelerate spuriously). This is even more true in the Arakawa scheme, at least theoretically (Grammeltvedt, 1969). However, these effects are not simple; in $N=40$ the phase angle suddenly changes almost discontinuously at the 7th day and in $N=80$ it happens at the 12th day.

c. *Zonal wind*

The zonal means of the west-east flow at level 3 (~189 mb) for the 1964 case are shown in Fig. 9. (In the observation, the data equatorward from 15N latitude are missing.)

It may be seen from these figures that: 1) the subtropic jet centered around 33N is too strong in all of the predictions; 2) the polar-frontal jet at about 70N is better represented by the $N=80$ model as was mentioned earlier; 3) after 12 days, the agreement between

the overall features of the prediction and observation becomes worse; 4) in the $N=20$ model, the subtropical jet shifts equatorward [see Manabe *et al.* (1970), although the effects of mountain and land-sea contrasts were not included in their model]; and 5) in the $N=80$ model, the subtropical jet shifts excessively poleward. Item 3) may be related to the limitation of the hemispheric model.

d. Verification scores

The prediction skill is assessed by comparing the 500- and 1000-mb geopotential heights with the observed over the domain north of 20N.

1) Standard deviation

We use the definition

$$[\Sigma(x-\bar{x})^2/n]^{\frac{1}{2}}$$

for the standard derivation, where n is simply the total number of grid points (map scale factor is omitted),

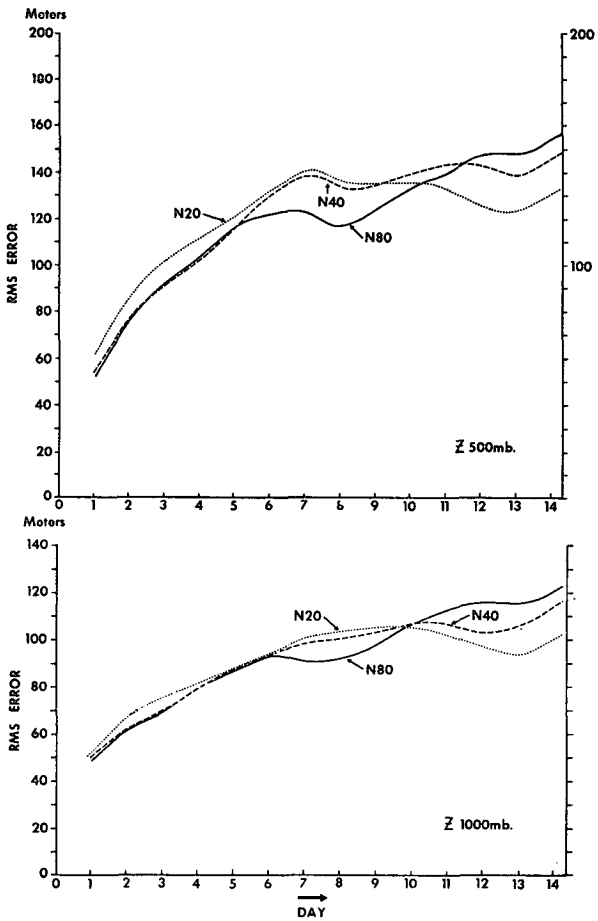

FIG. 10. The standard deviations of error of the predicted potential height at 500 and 1000 mb.

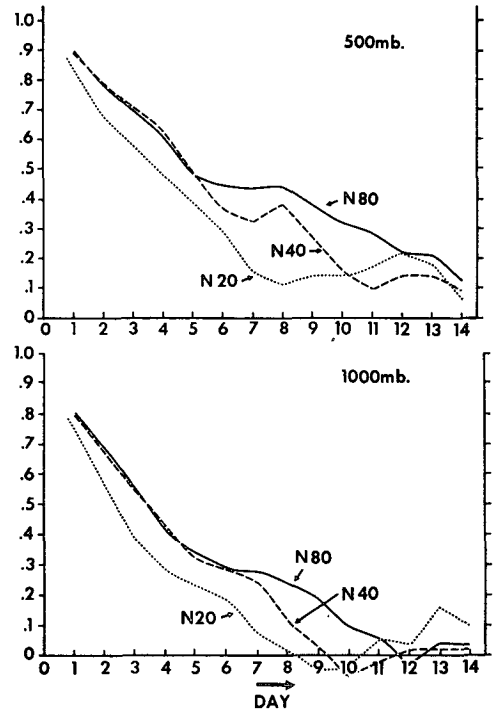

FIG. 11. The correlation coefficients between the observed and the predicted anomalies of geopotential heights for 500 and 1000 mb.

and $x=z_{\text{fcst}}-z_{\text{obs}}$, $\bar{x}=\Sigma x/n$, where z_{fcst} and z_{obs} are the forecast and observed heights.

Fig. 10 shows the time variation of the standard deviation which is the average for two cases, i.e., 1964 and 1966. The curves show that the results improve progressively with the increase of resolution after the 6th day and until the 10th day.

2) Correlation of geopotential anomaly

This is the correlation coefficient between the forecast and the observed height deviations from the January normal, z_{norm}, and is defined as

$$\frac{\overline{(Y_1-\bar{Y}_1)(Y_2-\bar{Y}_2)}}{[(Y_1-\bar{Y}_1)^2(Y_2-\bar{Y}_2)^2]^{\frac{1}{2}}},$$

where

$$Y_1(t)=z_{\text{obs}}(t)-z_{\text{norm}},$$
$$Y_2(t)=Z_{\text{fcst}}(t)-z_{\text{norm}}.$$

It is noted that the correlation used here is different from the one we used before (Miyakoda *et al.*, 1969), the previous one involving the time change from the initial height. Fig. 11 is the comparison of the correlation coefficients for 500- and 1000-mb geopotential height anomalies for the various horizontal resolutions. Two cases are averaged.

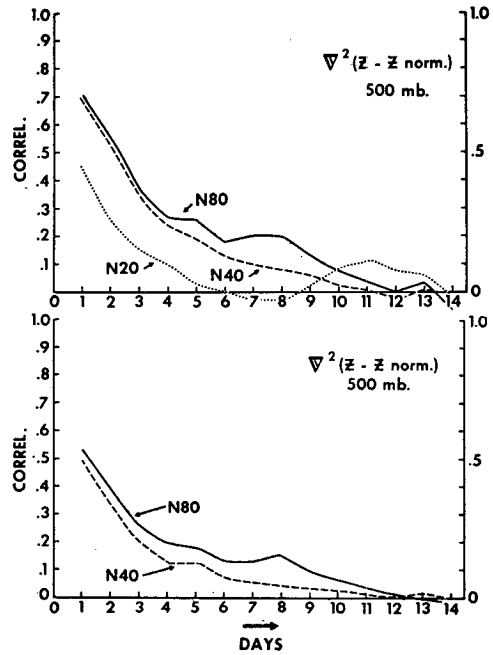

FIG. 12. The correlation coefficients between the observed and predicted Laplacian of geopotential anomalies for 500 mb. The upper part of the figure is based on the difference form of the Laplacian for $N=20$ and the lower for $N=40$.

The figure indicates that the $N=20$ result is clearly the worst; $N=40$ and $N=80$ are comparable at the beginning, but $N=80$ appears superior to $N=40$ after the 6th day and until the 11th day. The tendency is the same for the individual cases.

The hemispheric model has a limitation beyond a certain period. It appears after 8 days that the interaction between the mid-latitude and tropical zones becomes appreciable, and the performance of the hemispheric model becomes rather bad particularly after 12 days (see also Figs. 5–8).

3) Correlation of Laplacian of geopotential anomaly

The correlation for the geopotential height discussed above does not show all the details of the similarity of the height patterns. The coefficient may tend to place stress on a certain spectral range; that is, the planetary scale may affect the score disproportionately. Our interest is in the cyclone scale as well. In attempting to find a more sensitive measure of skill for the smaller pattern, we computed the correlation between the Laplacians of the observed and the forecast height anomalies (which correspond to the geostrophic vorticity).

The finite difference form of the Laplacian is

$$\nabla^2 X = X_{i+p,j} + X_{i-p,j} + X_{i,j+p} + X_{i,j-p} - 4X_{i,j},$$

where the subscripts i and j are the indices of the grid point for the x and y directions, respectively, and $X=z-z_{\text{norm}}$. Two kinds of differences for $\nabla^2 X$ were taken; one is the same grid size as $N=20$ and the other is that of $N=40$.

As seen in Fig. 12, the coefficients for $\nabla^2(z-z_{\text{norm}})$ are generally lower than those for $z-z_{\text{norm}}$. It is clear this time, however, that the superiority of the higher resolution model is apparent even from the 1st day. The score for the $N=20$ result drops very quickly. This indicates that the $N=80$ result is particularly good in the smaller scale features of the solution.

7. Features of the general circulation

a. Hemispheric average of temperature

It has been noticed that the model atmosphere is appreciably colder than the observed. This is true not only in the general circulation result in which a long-term integration is made for the condition of annual mean radiation (Manabe *et al.*, 1965, 1970), but also in the result of the 14-day real data prediction (Miyakoda *et al.*, 1969).

Fig. 13 shows the vertical distribution of temperature difference, i.e., computed minus observed, averaged over the domain north of 20N for the 14-day period (the 1964 case).

In the troposphere below level 4, the deficit decreases with the increase of grid resolution probably because more latent heat is released in the higher resolution model (see later). It evidently converges to a certain negative value (not zero), indicating that the model has other deficiencies which are partly responsible for this tendency.

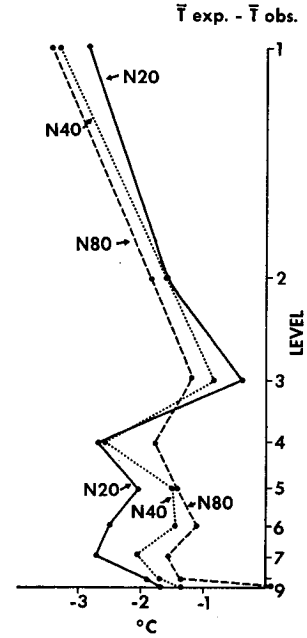

FIG. 13. The hemispherically averaged temperature error (computed minus observed).

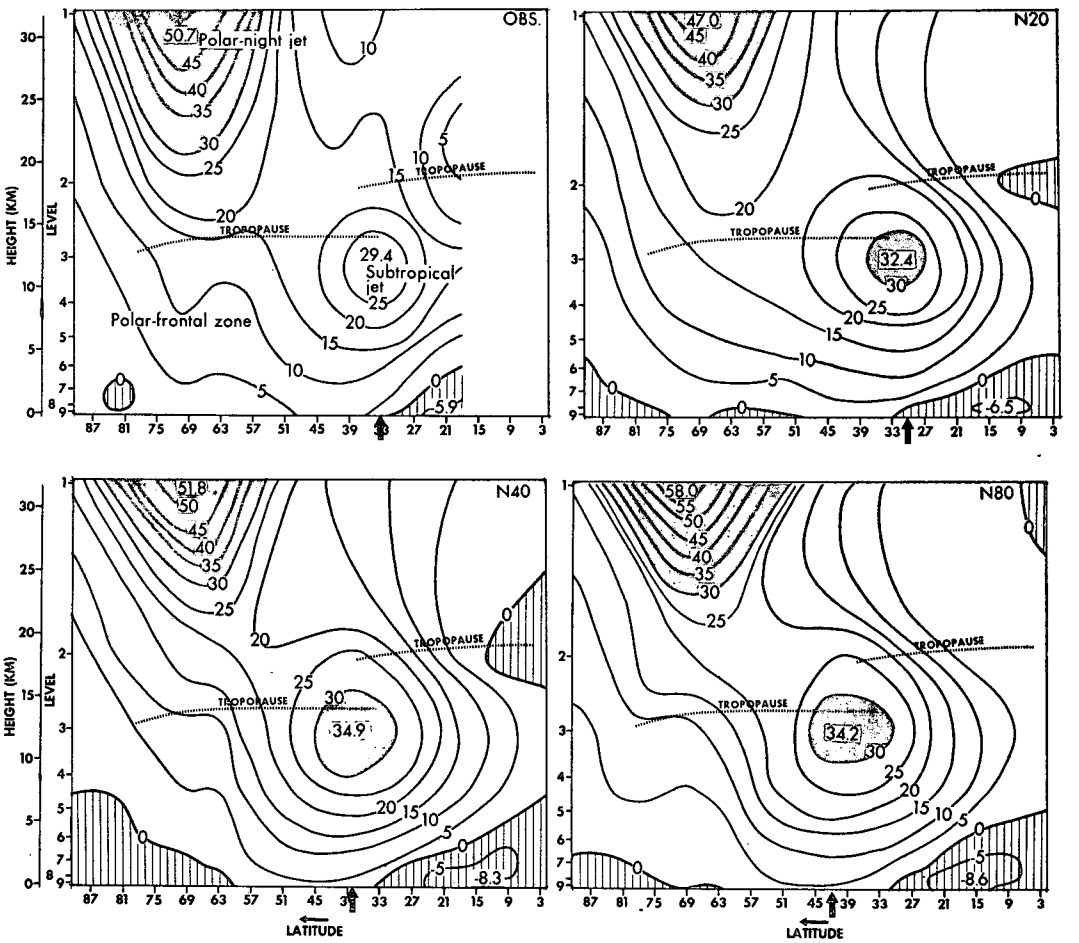

FIG. 14. Meridional sections of zonal wind (m sec^{-1}). The regions of westerlies with intensity >30 m sec^{-1} are stippled, and the easterlies are hatched. Extreme values are plotted. The arrows at the bottom indicate the position of the subtropical jet.

b. Meridional sections

1) Zonal wind

Fig. 14 illustrates the averaged zonal wind over the 14-day period. Let us, for convenience, divide the meridional section of the zonal flow into three parts, i.e., those centered around the subtropical, the polar-frontal, and the polar-night jets. It is known that one defect in the model's performance is that the subtropical westerlies are too strong compared to the observed. The present case is not an exception. The maximum intensity of the observed zonal flow in the subtropical jet at 39N (Fig. 10) is 29.4 m sec^{-1}, whereas the values in the predictions are greater than 32 m sec^{-1}.

Evidently the horizontal resolution does not cause a large variation in wind intensity (in agreement with Wellck *et al.*, 1971). We also made a separate test for vertical resolution, i.e., the $N=20$ (9-level) and the $N=20$ (18-level) models. The result shows that an increase of the vertical levels just increases the strength of the westerlies, giving a greater error. Thus, it is almost definite that other factors must be considered in order to reduce the jet intensity. The vertical diffusion of momentum is one factor that may be considered.

As was mentioned earlier, it is quite obvious that the position of the jet axis is shifted poleward in the $N=80$ case (the jet positions are indicated by arrows in Fig. 14).

The polar-frontal westerlies observed at 70N are simulated better in $N=80$. These westerlies have not been discussed much recently, but they certainly deserved more attention (see Palmén and Newton,1969).

2) Eddy kinetic energy

Fig. 15 is the zonal mean 14-day average of eddy kinetic energy , i.e.,

$$\int \frac{1}{2}\rho(\overline{u'^2}+\overline{v'^2})d\lambda/(2\pi),$$

λ being the longitude. This is one of the quantities which is most difficult to predict and yet most important for extended-range forecasts.

The improvement of this variable with increase of

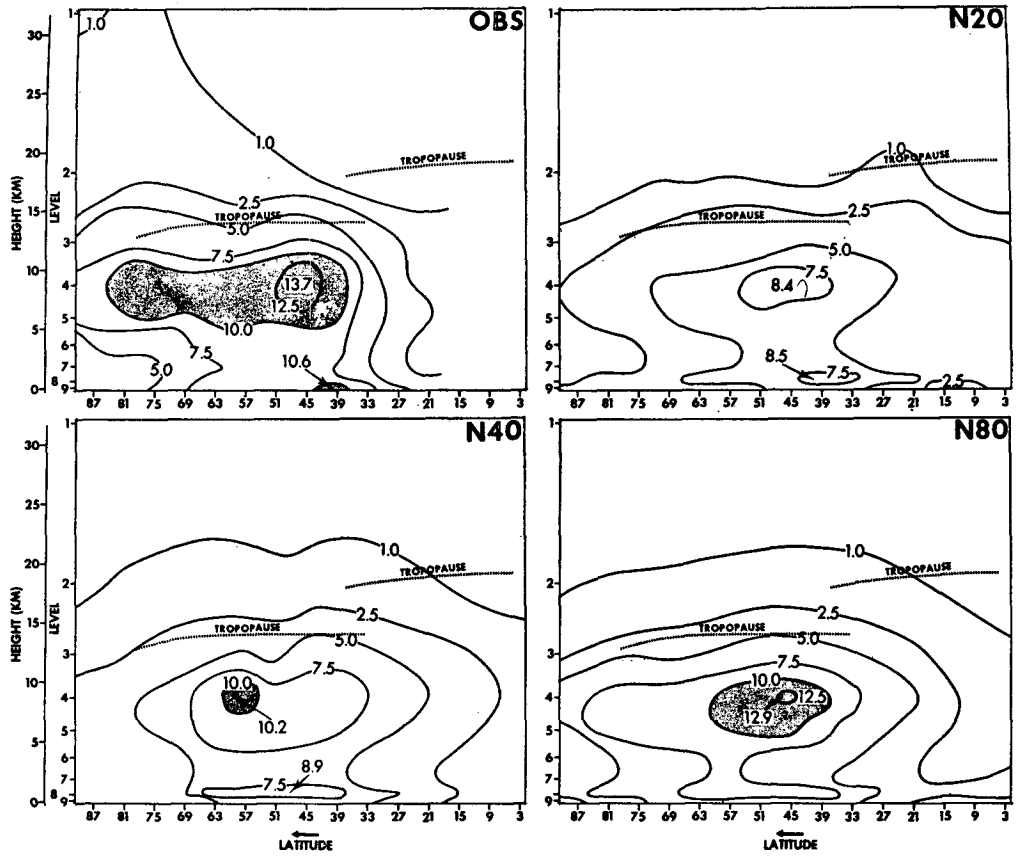

FIG. 15. Meridional sections of eddy kinetic energy, $\rho(\overline{u'^2}+\overline{v'^2})/2$, in units of 10^2 ergs cm^{-3}. The regions where the intensity $>10^3$ ergs cm^{-3} are stippled. The maxima are plotted.

resolution is large. The maximum observed value of K_E is 13.7×10^2 ergs cm^{-3}, and the area of large values extends to the polar frontal region. The maximum values in the predictions are 8.4×10^2, 10.2×10^2 and 12.9×10^2 ergs cm^{-3} for $N=20$, $N=40$ and $N=80$, respectively. However, even the result for $N=80$ is not sufficient. It should be remembered that the eddy coefficient k_0 is also related to this problem.

c. Eddy transfer

Fig. 16 gives the results for the eddy meridional transfer of angular momentum,

$$\int \rho 2\pi a \cos\varphi \overline{v'm_A'}dz \Big/ \int \rho dz,$$

and the eddy meridional transfer of sensible heat,

$$\int \rho 2\pi a C_p \cos\varphi \overline{v'T'}dz \Big/ \int \rho dz,$$

where

$$m_A = a\cos\varphi(a\cos\varphi\cdot\Omega+u)$$

is the angular momentum. All quantities are averaged in the zonal direction around the globe (the bar notation), and integrated vertically and averaged for the period of two weeks. The curves are the average of two January cases.

The results may be self-explanatory. It is, however, noteworthy that the maxima of transfer of momentum and heat in the $N=80$ solution are shifted poleward compared with the observed. The agreement is rather worse for $N=80$ than for $N=40$. The same quantities are also shown by Manabe *et al.* (1970) with respect to a general circulation experiment which did not include the mountains or the land-sea distribution.

d. Condensation of water vapor

Fig. 17 shows the zonal means of the computed condensation averaged over 14 days, for the two cases. It is seen from this figure that 1) the amount of condensation increases with resolution, and 2) the mid-latitude maximum for the $N=20$ model is shifted equatorward, reflecting the latitudinal position of the subtropical jet.

Another important aspect related to condensation concerns the humidity criterion. As discussed in the 1969 paper, the criterion may be a function of the grid size and should be smaller than the continuum limit of 100% for effective resolution.

In the present experiments, we assumed the criterion

to be 80% everywhere for all three grids. Fig. 18 compares the humidity distribution for each grid size with the observation for the 1964 case. This indicates, as was speculated, that humidity decreases with an increase of resolution at middle and high latitudes. The 80% criterion is perhaps too low for levels 7 and 8 in the $N=80$ model, and may also be a function of height, i.e., increasing with decreasing altitude (see Smagorinsky, 1960; Gadd and Keers, 1970).

8. Conclusions

The horizontal eddy viscosity coefficient we used for the nonlinear viscosity terms, $k_0=0.25$, seems large, and it probably should be reduced to about 0.1 or less. The lower viscosity produces cut-off lows more easily and increases the eddy kinetic energy but the formation of a new trough can hardly be expected from a simple reduction of viscosity.

On the other hand, an increase of horizontal grid resolution can correctly give rise to a new trough or ridge which is missed by a lower resolution model.

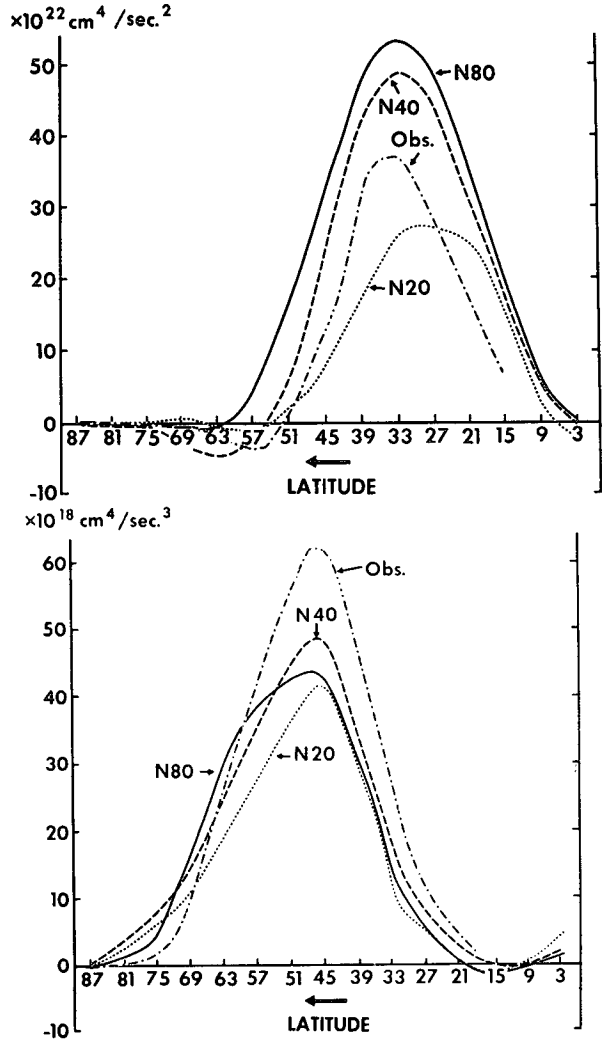

FIG. 16. Meridional transfer of eddy angular momentum (upper) and of sensible heat (lower).

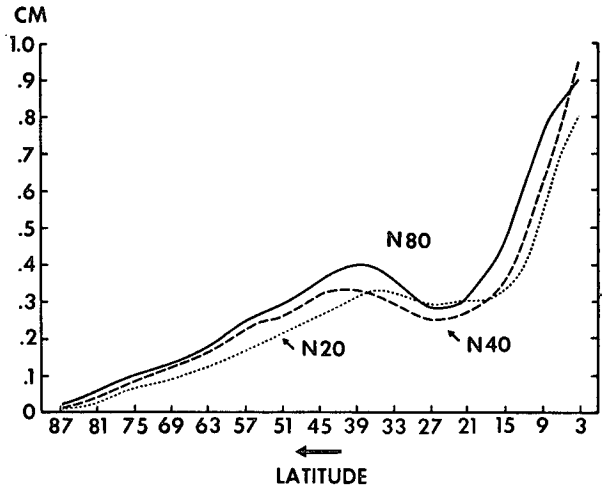

FIG. 17. Latitudinal distribution of precipitation.

The effects of grid size on the two-week evolution of atmospheric motion were studied. The differences between the $N=20$ and $N=40$ solutions are, in many respects, substantial. The $N=20$ forecast is inferior; the predicted day-to-day variation of weather systems is practically unacceptable.

On the other hand, the difference between the $N=40$ and $N=80$ solutions is not particularly large for the first 5 days for scales larger than that of cyclones, but the difference is sizable after 5–6 days. It should be stressed, however, that there is appreciable improvement even from the first day in the smaller scale features of the flow; the $N=80$ result is better than $N=40$ in the distribution of geostrophic vorticity.

Analysis based on two winter cases revealed the following improvements beyond the 6th day, associated with refining the mesh from $N=40$ to $N=80$. Appreciably improved are the 1000-mb geopotential field, the behavior and intensity of polar fronts, and the intensity of eddy kinetic energy. It is particularly worthy mentioning that long waves are better predicted in $N=80$ model than in $N=40$ model. Some improvements are noticed in the verification score of 500- and 1000-mb height patterns, and the hemispheric mean temperature. Some difference is noticed in the amount of precipitation in the tropics as well as in mid-latitudes.

Defects are also noticed in $N=80$ model compared with $N=40$. First, the wiggling in the flow field is stronger partly due to the effective reduction of viscosity dissipation and partly to the nature of convective adjustment. Second, the breakdown of the solution beyond the 12th day (possibly due to the equatorial boundary in the hemispheric model) is more clearly noticeable in $N=80$ model. Third, the latitudinal position of the subtropical jet is somewhat shifted poleward in $N=80$ solution.

Nevertheless, in order to extend the prediction range

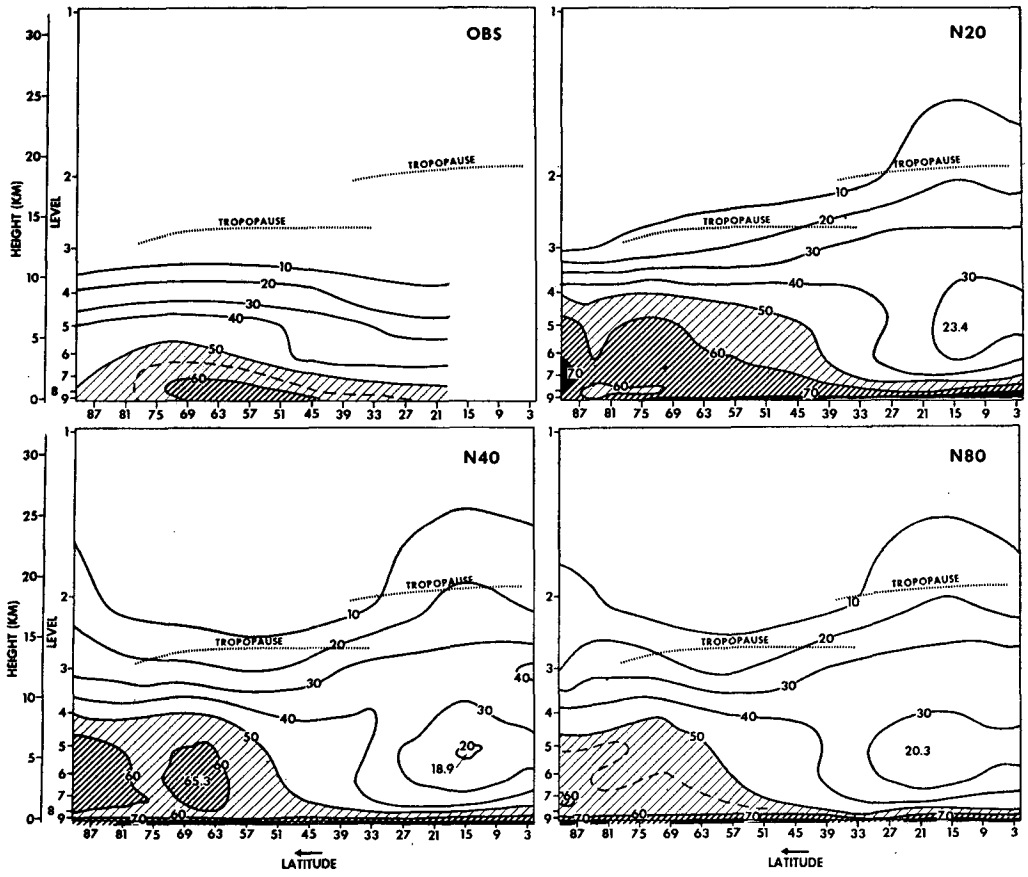

FIG. 18. Meridional sections of relative humidity (percent).

beyond 6 days, the $N=80$ grid is needed, for the long wave, at least for the finite-difference scheme which is presently used.

It is also demonstrated that the computed distribution of humidity varies appreciably and systematically with resolution of the model.

Acknowledgments The authors are grateful to Dr. J. Smagorinsky for his interest and encouragement. Special thanks are due also to Drs. Y. Kurihara, S. Manabe and T. Matsuno, and to Messrs. H. Frazier, D. Gauntlett, D. Hincksman, J. L. Holloway, Jr., D. Johnson, T. Mauk, S. Porter, I. Shulman and Mrs. Y. Towns for suggestions, criticisms and technical assistance.

REFERENCES

Arakawa, A. 1966: Computational design for long-term numerical integrations of fluid motion: Two-dimensional incompressible flow. Part I. *J. Comput. Phys.*, **1**, 119–143.

Benwell, G. R. R., and F. H. Bushby, 1970: A case study of frontal behavior using a 10-level primitive equation model. *Quart. J. Roy. Meteor. Soc.*, **96**, 287–296.

Bryan, K., 1966: A scheme for numerical integration of the equations of motion on an irregular grid free of nonlinear instability. *Mon. Wea. Rev.*, **94**, 39–40.

Bushby, F. H., and M. S. Timpson, 1967: A 10-level atmospheric model and frontal rain. *Quart. J. Roy. Meteor. Soc.*, **93**, 1–17.

Charney, J. G., and A. Eliassen, 1949: A numerical method for predicting the perturbations of the middle-latitude westerlies. *Tellus*, **1**, No. 2, 38–54.

——, R. Fjørtoft and J. von Neumann 1950: Numerical integration of the barotropic vorticity equation. *Tellus*, **2**, 237–254.

Cressman, G. P., 1958: Barotropic divergence and very long atmospheric waves. *Mon. Wea. Rev.*, **86**, 293–297.

Deardorff, J. W., 1971: On the magnitude of the sub-grid scale eddy coefficient. *J. Comput. Phys.*, **7**, 120–133.

Deland, R. J., 1964: Travelling planetary waves. *Tellus*, **16**, 271–273.

——, 1965: Some observations of the behavior of spherical harmonic waves. *Mon. Wea. Rev.*, **93**, 307–312.

Derome, J., and A. Wiin-Nielsen, 1971: The response of a middle latitude model atmosphere to forcing by topography and stationary heat sources. (To be published.)

Döös, B. R. 1962: The influence of exchange of sensible heat with the earth's surface on the planetary flow. *Tellus*, **14**, 133–147.

Eliassen, E., and B. Machenhauer, 1965: A study of the fluctuations of the atmospheric planetary flow patterns represented by spherical harmonics. *Tellus*, **17**, 220–238.

Fjørtoft, R., 1953: On the changes in the spectral distribution of kinetic energy for two-dimensional non-divergent flow. *Tellus*, **5**, 225–230.

Gadd, A. J., and J. F. Keers, 1970: Surface exchanges of sensible and latent heat in a 10-level model atmosphere. *Quart. J. Roy. Meteor. Soc.*, **96**, 297–308.

Gerrity, J. P., Jr., and R. D. McPherson, 1969: Development of a limited area fine-mesh prediction model. *Mon. Wea. Rev.*, **97**, 665–669.

Gilchrist, B., 1953: Seasonal phase changes of thermally produced perturbations in the westerlies. *Proc. Toronto Meteor. Conf.*, Amer. Meteor. Soc. and Roy. Meteor. Soc., 129–131.

Grammeltvedt, A., 1969: A survey of finite-difference schemes for the primitive equations for a barotropic fluid. *Mon. Wea. Rev.*, **97**, 384–404.

Howcroft, J. G., 1966: Fine-mesh limited area forecasting model. Air Weather Service Tech. Rept. 188, 71–75.

Kao, S.-K., and L. L. Wendell, 1970: The kinetic energy of the large-scale atmospheric motion in wavenumber-frequency space. *J. Atmos. Sci.*, **27**, 359–375.

Knighting, E., 1960: On the grid length to be adopted in numerical weather prediction. *Quart. J. Roy. Meteor. Soc.*, **86**, 265–270.

Kubota, S., and S. Iida, 1954: Statistical characteristics of the atmospheric disturbances. *Papers Meteor. Geophys., Tokyo*, **5**, No. 1, 22–34.

Kurihara, Y., 1965: On the use of implicit and iterative methods for the time integration of the wave equation. *Mon. Wea. Rev.*, **93**, 33–46.

Leith, C. E., 1968: Diffusion approximation for two-dimensional turbulence. *Phys. Fluids*, **11**, 671–674.

Lilly, D. K., 1967: The representation of small-scale turbulence in numerical simulation experiments. *Proc. IBM Scientific Computing Symposium on Environmental Sciences*, IBM Form No. 320-1951, 145–210.

——, 1970: Numerical simulation of developing and decaying two-dimensional turbulence. NCAR Manuscript No. 69-178.

Magata, M., 1957: On the truncation errors in numerical prediction. *Papers Meteor. Geophys., Tokyo*, 8, 133–143.

Manabe, S., J. Smagorinsky and R. F. Strickler, 1965: Simulated climatology of a general circulation model with a hydrologic cycle. *Mon. Wea. Rev.*, **93**, 769–978.

——, ——, J. L. Holloway, Jr. and H. M. Stone, 1970: Simulated climatology of a general circulation model with a hydrologic cycle. III. Effects of increased horizontal computational resolution. *Mon. Wea. Rev.*, **98**, 175–212.

Martin, D. E., 1958: An investigation of the systematic errors in the barotropic forecasts. *Tellus*, **10**, 451–465.

Matsuno, T., 1966: Numerical integrations of primitive equations by use of a simulated backward difference method. *J. Meteor. Soc. Japan*, 44, 76–84.

Mintz, Y., 1965: Very long term global integration of the primitive equations of atmospheric motion. Geneva, World Meteor. Organization, Tech. Note No. 66, 141–167.

Miyakoda, K., 1960: A trial of 500 hour barotropic forecast. *Proc. Intern. Symp. Numerical Weather Prediction*, Tokyo, Meteorological Society of Japan, 221–240.

——, J. Smagorinsky, R. F. Strickler and G. D. Hembree, 1969: Experimental extended predictions with a nine-level hemispheric model. *Mon. Wea. Rev.*, **97**, 1–76.

——, and Staff Members, 1968: Extended prediction with a nine-level model on the Kurihara grid. *Proc. WMO/IUGG Symp. Numerical Weather Prediction*, Tokyo.

Murakami, T., 1956: The topographical effect upon the stationary upper flow patterns. *Papers Meteor. Geophys., Tokyo*, **7**, 69–89.

——, 1964: The topographic effects in the three-level model of the s-coordinate *Papers Meteor. Geophys., Tokyo*, **14**, 144–150.

Økland, H., 1958: False dispersion as a source of integration errors. Sci. Rept., No. 1, Det. Norske Meteorologiske Institut, Oslo.

Ogura, Y., 1958: On the isotropy of large-scale disturbances in the upper troposphere. *J. Meteor.*, **15**, 375–382.

Palmén, E., and C. W. Newton, 1969: Atmospheric circulation systems: Their structure and physical interpretation. *International Geophysics Series*, Vol. 13, New York, Academic Press, 603 pp.

Phillips, N. A., 1956: The general circulation of the atmosphere: A numerical experiment. *Quart. J. Roy. Meteor. Soc.*, **82**, 123–164.

——, 1959: An example of non-linear computational instability. *The Atmosphere and the Sea in Motion*, New York, The Rockfeller Institute Press, 501–504.

——, 1963: Geostrophic motion. *Rev. Geophys.*, **1**, 123–176.

Platzman, G. W., 1961: An approximation to the product of discrete functions. *J. Meteor.*, **18**, 31–37.

——, 1968: The Rossby wave. *Quart. J. Roy. Meteor. Soc.*, **94**, 225–248.

Reiser, H., 1957: On the introduction of centered finite-difference quotients in atmospheric prediction models. *Studies in Numerical Weather Forecasting*. Frankfurt/Main, Deutscher Wetterdienst.

Reiter, E. R., 1958: Die Verwendung von Kontinuitätsdiagrammen in der nordalpinen Wetterprognose. *Arch. Meteor. Geophys. Bicklim.*, **A10**, 161–177.

Rossby, C.-G., 1945: On the propagation of frequencies and energy in certain types of oceanic and atmospheric waves. *J. Meteor.*, **2**, 187–204.

Saltzman, B., 1959: On the maintenance of the large-scale quasi-permanent disturbances in the atmosphere. *Tellus*, **11**, 423–431.

——, 1962: Spectral statistics of the wind at 500 mb. *J. Atmos. Sci.*, **19**, 195–206.

——, 1963: A generalized solution for the large-scale, time-average, perturbations in the atmosphere. *J. Atmos. Sci.*, **20**, 226–235.

——, and A. Fleisher, 1960: The exchange of kinetic energy between larger scales of atmospheric motion. *Tellus*, **12**, 374–377.

Sankar-Rao, M., 1965: Continental elevation influence of the stationary harmonics of the atmospheric motion. *Pure Appl. Geophys.*, **50**, 141–159.

——, and B. Saltzman, 1969: On a steady state theory of global monsoons. *Tellus*, **21**, 308–330.

Shuman, F. G., 1960: Numerical experiments with the primitive equations. *Proc. Intern. Symp. Numerical Weather Prediction*, Tokyo, Meteorological Society of Japan, 85–107.

Smargorinsky, J., 1953: The dynamical influence of large-scale heat sources and sinks on the quasi-stationary mean motion of the atmosphere. *Quart. J. Roy. Meteor. Soc.*, **79**, 342–366.

——, 1960: On the dynamical prediction of large-scale condensation by numerical methods. *Geophys. Monogr.*, No. 5, Amer. Geophys. Union, 71–78.

——, 1963: Genreal circulation experiments with the primitive equations: I. The basic experiment. *Mon. Wea. Rev.*, **91**, 99–164.

——, S. Manabe and J. L. Holloway, Jr., 1965: Numerical results from a nine-level general circulation model of the atmosphere. *Mon. Wea. Rev.*, **93**, 727–768.

Staff Members, Academia Sinica, 1958: On the general circulation over Eastern Asia, IV. *Tellus*, **10**, 299–312.

van Loon, H., 1965: A climatological study of the atmospheric circulation in the Southern Hemisphere during the IGY, Part I: 1 July 1957–31 March 1958. *J. Appl. Meteor.*, 4, 479–491.

Wellck, R., A. Kasahara, W. Washington and G. DeSanto, 1971: The effect of horizontal resolution in a finite-difference model of the general circulation. *Mon. Wea. Rev.* (in press).

Wiin-Nielsen, A., 1959: On barotropic and baroclinic models with special emphasis on ultra-long waves. *Mon. Wea. Rev.*, **87**, 171–183.

Wolff, P. M., 1958: The error in numerical forecasts due to retrogression of ultra-long waves. *Mon. Wea. Rev.*, **86**, 245–250.